Origin of protons accelerated by an intense laser and the dependence of their energy on the plasma density

Takashi Nakamura*

Department of Environmental Sciences and Technology, Tokyo Institute of Technology, 4259 Nagatsuta, Yokohama 226-8502, Japan

Shigeo Kawata†

Department of Electrical and Electronic Engineering, Utsunomiya University, 7-1-2 Yoto, Utsunomiya 321-8585, Japan

We study the high-energy (1–4 MeV) proton production from a slab plasma irradiated by a ultrashort high-power laser. In our 2.5-dimensional particle-in-cell simulations, a *p*-polarized laser beam of 1.6×10^{19} W/cm^2, 300 fs, $\lambda_L = 1.053$ μm, illuminates a slab plasma normally; the slab plasma consists of a hydrogen plasma, and the target plasma thickness and the laser spot size are $2.5\lambda_L$ and $5\lambda_L$, respectively. The simulation results show that an emitted proton energy depends on the slab plasma density, and three kinds of high-energy proton beams are generated at the target plasma surfaces: one kind of the proton beams is produced at the laser-illuminated target surface and accelerated to the same laser-incident side. The second is generated at the target surface opposite to the laser-illuminated target surface and is accelerated outward on the same side. The third is generated at the laser-illuminated target surface and accelerated to the opposite side while passing through the target plasma. The simulations also show a mechanism of proton accelerations. In an overdense plasma, laser energy goes to energies of hot electrons and magnetic fields in part; the electrons oscillate around the slab plasma so that a static electric field is generated and consequently protons are extracted. The magnetic field generated in the slab plasma exists longer and heats up the plasma electrons to sustain the static electric field even after the laser termination.

I. INTRODUCTION

In recent years, interaction between high-intensity laser and matter has been studied actively. Especially, series of experiments carried out at Lawrence Livermore National Laboratory (LLNL) [1], University of Michigan [2] and Rutherford Appleton Laboratory [3] using an ultrahigh intensity laser system are very interesting from a scientific and engineering points of view. In the experiments, a thin film consisting of aluminum or CH polymer was irradiated with an intense ultrashort pulse laser, and the generation of high-energy protons was observed. The proton energy reaches about 1–10 MeV. If such a high-energy-ion generation is established and its mechanism is clarified, new scientific world may be opened in the fields of ion sources for particle accelerators, inertial confinement fusion applications, and so on [4–9].

In this paper, we study the high-energy proton production from slab hydrogen plasma irradiated by an ultrashort high-power laser by 2.5-dimensional particle-in-cell (PIC) simulations [10–14] in order to investigate the dependence of the proton energy on a target slab plasma density, a mechanism of proton acceleration and origin of high-energy protons in a target. In the particle simulations carried out in this paper, the initial plasma density n_f is selected between the critical den-

*Electronic address: tnaka@depe.titech.ac.jp; URL http://fa.depe.titech.ac.jp/

†Electronic address: kwt@cc.utsunomiya-u.ac.jp; URL http://skkd1.ee.utsunomiya-u.ac.jp/

sity n_c and $10n_c$. A *p*-polarized laser beam of 1.6×10^{19} W/cm^2, 300 fs, $\lambda_L = 1.053$ μm, illuminates a slab plasma normally; the slab plasma consists of a hydrogen plasma and the target plasma thickness and the laser spot size are $2.5\lambda_L$ and $5\lambda_L$, respectively.

The simulation results show a mechanism of proton accelerations clearly and will be discussed in detail in Sec. III. During the laser illumination, electrons existing around the laser-irradiated surface are accelerated violently. The generation of energetic hot electrons causes a spatial charge separation on the irradiated target surface. Simultaneously, some electrons pass through the target slab plasma and run away into the vacuum from the target surface opposite to the laser-irradiated surface. Then the electrons oscillate around the slab plasma and create the charge separation on both the target surfaces. The charge separation in the narrow spatial region results in a generation of strong electrostatic field (ESF) which reaches up to MV/μm [2]. Then, the generated ESF accelerates the protons existing in the narrow regions on the target surfaces [15,16]. By a series of the simulations, it is found that the proton energy emitted depends on the slab plasma density and there is an optimal plasma density for the proton acceleration, and that the efficient and continuous energy transfer to the electrons is a crux to determine the final maximum energy of the accelerated protons, because the electrons cause the charge separation and sustain the strong ESF to accelerate the protons. In this connection, it is also found that the excitation of the strong inner magnetic field inside the target is important for the continuous energy transfer to the electrons from the magnetic field, as well as the efficient energy deposition of the laser in the electrons. For

$n_f \gtrsim n_c$, an excitation of a strong magnetic field inside the target plasma is observed, in addition to the surface magnetic field excited on the target surface due to the hot electron generation. This inner magnetic field inside the plasma is excited by the electron flow traversing the slab plasma from the laser-illuminated surface to the other surface due to the ponderomotive force during the laser illumination. The amplitude of the inner magnetic field reaches about 10^3 T. After the laser illumination ends, the inner magnetic field breaks into small scale structures by a collision with the surface magnetic field on the target surface and heats the electrons continuously.

Furthermore, the simulation results show the origin of the high-energy protons generation. It was suggested that the protons are generated from hydrocarbons or vapors contaminating a thin layer on the target surface [17–19], and it was observed that the energetic protons are generated from a thin layer on the surfaces in the recent high-intensity ultrashort experiments [1–3]. In this paper, the simulation results also show that the high-energy protons are generated at the narrow layers on the two surfaces of the slab plasma: one is the laser-illuminated surface and the other is the surface opposite to the laser-illuminated surface. While most of the protons generated at the surfaces are accelerated outward, it is also reconfirmed that some energetic protons generated from the laser-illuminated surface are accelerated while passing through the target and go out of the opposite side of the laser-incident side as suggested by previous works [2,4,20]. Furthermore, in this work, it is found that this crossing-proton generation is accompanied by the excitation of the magnetic field in the inside of plasma, while passing through the plasma.

In Sec. II, we describe the computational model and a complete parameter set used in the 2.5-dimensional PIC simulations. In Sec. III, simulation results are presented and the dependence of the proton energy on the target plasma density is described. Then, a mechanism of proton acceleration and the origin of the high-energy protons are also investigated. In Sec. IV, a summary is presented.

II. SIMULATION MODEL

Figure 1 shows the schematic view of the simulation model for the two-dimensional $3V((X,Y),(v_x,v_y,v_z))$-electromagnetic PIC simulation. For simplicity, a uniformity in the z direction is assumed in this paper. In the simulation, all quantities depend on the X and Y coordinates and on time.

In the experiments [1–3], it was found that the predominant component of the high-energy ions emitted is proton, and the protons are generated at the thin layer on the target surface contaminated with a vapor and hydrocarbon, while a thin film of aluminum or CH polymer is used as a target. In this paper, we employ a thin film consisting of a slab hydrogen plasma for simplicity, so that we devote ourselves into investigations of the dependence on the target density and the origin of these protons. The interaction between the laser and the hydrogen slab plasma is computed. The plasma thickness δ_f is $2.5\lambda_L$. The simulations are carried out with the eight different slab plasma densities: n_f
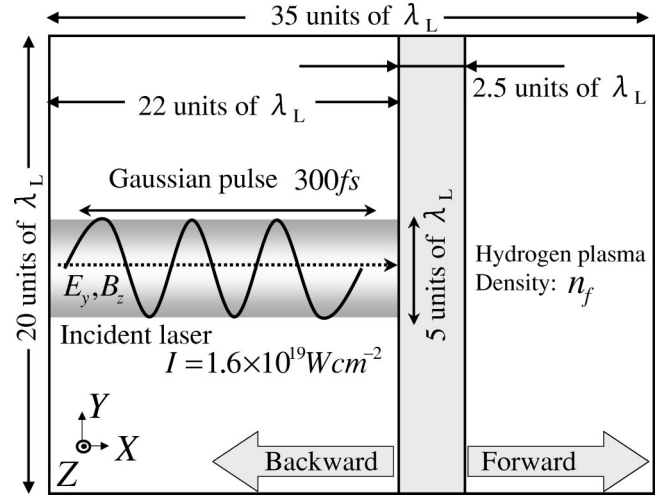

FIG. 1. A schematic view of the 2.5-dimensional particle-in-cell simulation model. The computational domain is given by $R = \{(x,y)|0<x<35\lambda_L, 0<y<20\lambda_L\}$. At the initial time ($t=0$), a slab plasma is placed in $22\lambda_L \leq x \leq 24.5\lambda_L$ with the density n_f and the other computational region is in the vacuum. A plane p-polarized laser illuminates a slab plasma normally. The laser-illuminated side and another opposite side are indicated by "backward" and "forward," respectively. In this paper, the uniformity in the z direction is assumed. The laser spot size is $r_{spot}=5\lambda_L$ and the laser has the Gaussian profile in both the x and y directions.

$=n_c, 2n_c, 3n_c, 4n_c, 8n_c$, and $10n_c$. Here, in the present paper, we use $\lambda_L = 1.053$ μm. Thus, δ_f and n_c are estimated to be $\delta_f = 2.51$ μm and $n_c = (2\pi)^2 m_e / \mu_0 e^2 \lambda_L^2 = 1.01 \times 10^{21}$ cm^{-3}, respectively. The plasma consists of the protons and electrons and the plasma charge is neutral initially. The electrons and protons are in the Maxwell distributions with the temperatures $T=0.1$ keV at the initial time. The ion mass used in the simulations is $1836m_e$.

A plane p-polarized laser of a wavelength $\lambda_L = 1.053$ μm illuminates a slab plasma normally. At the start of $t=0$, the incident electromagnetic laser wave enters from the left boundary ($x=0$), and the time development of the electric fields E_x, E_y and magnetic field B_z are calculated according to the Maxwell equation. The laser entering the computational domain has the Gaussian profile in both the transverse and longitudinal directions. The center of the Gaussian profile in the transverse direction is $y_c = 10\lambda_L$ and the spot size is $r_{spot} = 5\lambda_L$. The duration of the laser is $\tau = 300$ fs and the amplitude of the entering laser is determined so that the peak intensity is equal to 1.6×10^{19} W/cm^2 in vacuum.

Initially 700 000 electron-proton pairs are loaded into the computational domain. In the computations, the relativistic equation of motion of the protons and electrons, and the Maxwell equations are solved in the program self-consistently [10–12]. The Cartesian mesh system supplemented with a uniform mesh width is used. The mesh width in the X and Y directions, Δx and Δy are set to be equal $\Delta x = \Delta y = \Delta$, where Δ is determined for each n_f so that the skin depth of the incident laser δ_{skin} is smaller enough than
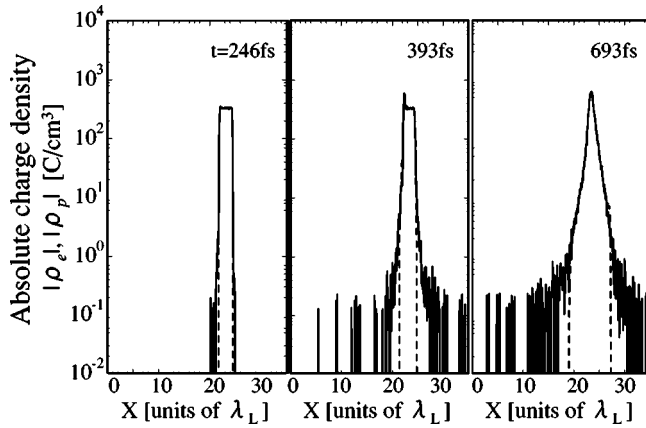
FIG. 2. Time development of the charge distribution in the x direction for $n_f = 2n_c$. The absolute charge densities averaged in the y direction over $|y - y_c| < r_{spot}$ are presented, and solid curves represent the electron charge density and dashed curves the proton charge density.

the spatial mesh width Δ. For example, in the case of $n_f = 4n_c$, the spatial grid widths in the X and Y direction are set to be $\Delta = 0.035\lambda_L (= \Delta_x = \Delta_y)$, while the skin depth is estimated as $\delta_{skin} \cong 0.1\lambda_L$. According to the mesh width, the computational time interval Δt is determined by $\Delta t = 0.04\Delta$ in each computation.

III. SIMULATION RESULTS

In this section, the numerical results are shown for the various densities of the target slab plasma, and we clarify the dependence of the high-energy proton generation on the
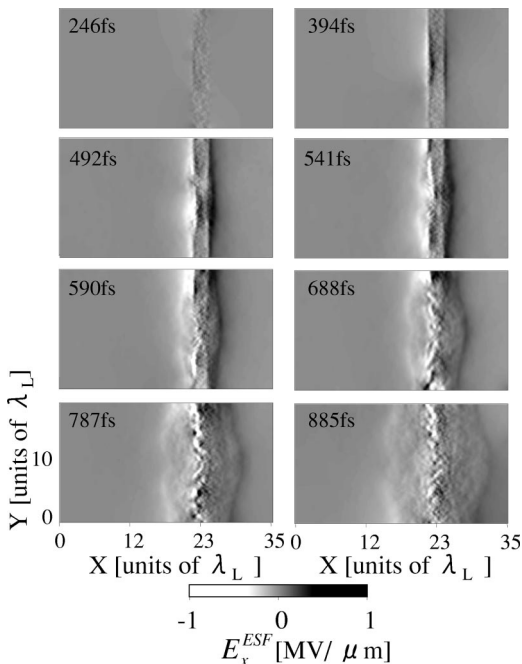

FIG. 3. Time development of the electrostatic field for $n_f = 2n_c$. The x component of the electrostatic field E_x^{ESF} is represented.
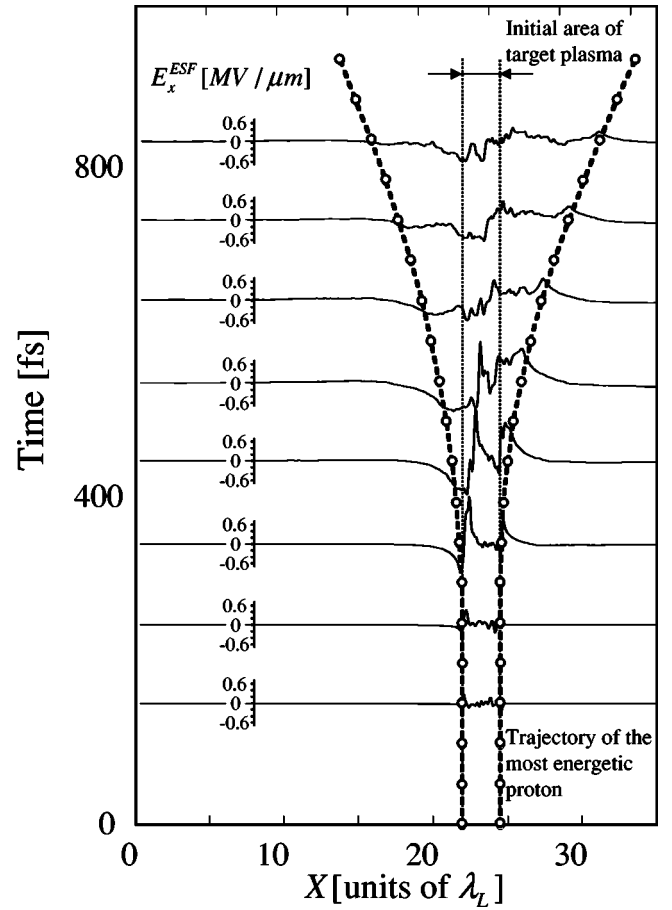

FIG. 4. The time evolution of the electrostatic field E_x^{ESF}, averaged in the y direction over $|y - y_c| < r_{spot}$, for $n_f = 2n_c$. White circles and dashed lines represent the trajectories of the most energetic protons in the backward and forward directions.

plasma density n_f. Hereafter, the laser-illuminated side and the other opposite side are indicated by the "backward" and "forward" sides, respectively, in order to distinguish the two sides, as shown in Fig. 1.

A. Proton acceleration by the ESF

Right after the laser initiation, the strong field of the incident laser accelerates a part of the electrons. These energetic electrons run away into the vacuum from both the sides of the target and the space charge separation appears on both the target surfaces. Figure 2 shows the distribution of the charge density in the x direction for $n_f = 2n_c$ and the density is averaged along the y axis. The dashed and solid curves represent the absolute charge density of the protons $|\rho_p|$ and the electrons $|\rho_e|$, respectively. In the figure, $|\rho_p|$ and $|\rho_e|$ are plotted in a logarithmic scale, so that ragged profile of $|\rho_e|$ appears at the low-density regions due to the finiteness of the number of used computational particles. The charge separation causes the strong electrostatic field of ~ 1 MV/μm around the plasma surface, and the protons existing around the surfaces are accelerated. Figure 3 shows the time evolution of the x component of ESF, E_x^{ESF} for $n_f = 2n_c$. E_x^{ESF} is estimated by solving the Poisson equation
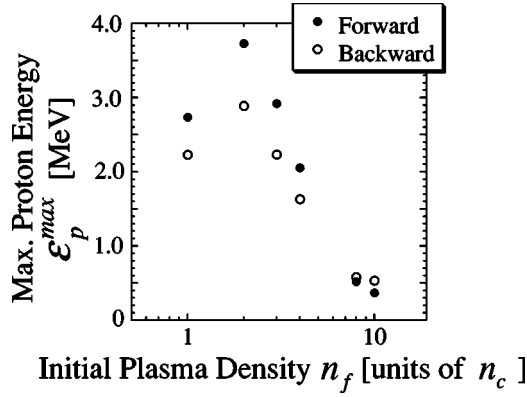
FIG. 5. The maximum kinetic energy ε_p^{max} of the protons emitted in the forward (black circles) and backward (white circles) directions as a function of the initial plasma density n_f.

$\nabla \cdot \mathbf{E}^{ESF} = (\rho_p - \rho_e)/4\pi\varepsilon_0$ at each computational time step. It is observed that the strong ESF is created by the charge separation at the initial acceleration phase and the sheets of the ESF propagate outward rapidly. When $n_f = 2n_c$, the maximum value of the amplitude of E_x^{ESF} reaches 0.644 MV/μm and 0.446 MV/μm for the forward and backward sides, respectively.

Figure 4 shows the time evolution of the x component of ESF averaged in the y axis for $n_f = 2n_c$. The white circles and dashed lines represent the trajectory of the proton that is accelerated to the highest energy, and the dotted lines represent the initial position of the target plasma. The electrostatic field propagates to the outward directions as time passes. It is verified that the protons, existing on the target surface at the initial time, move together with the E_x^{ESF} wave. Thus, the

protons are kept staying at the same phase of the propagating ESF wave and then accelerated effectively to the high energy. The energetic electrons, which are accelerated by the laser, escape from the slab plasma and exist beyond the protons. This situation is similar to a relation between an anode and a cathode in a high-power diode. Thus, the energetic electrons deposit their energy in the protons through the ESF that is caused by the charge separation. Therefore, the amplitude of the ESF and the number of the electrons sustaining the charge separation are important factors for the effective proton acceleration.

B. Dependence on the plasma density

Figure 5 shows the dependence of the resulting maximum kinetic energy of the proton ε_p^{max} on the target density n_f. ε_p^{max} depends on the initial slab plasma density clearly and there is an optimal in the plasma density for the proton acceleration. In both the forward and backward directions, the maximum proton energy is observed at $n_f = 2n_c$. In the optimal density, the protons emitted to the forward and the backward are accelerated to 3.73 MeV and 2.89 MeV, respectively. The highest energy of the protons in the backward direction is slightly smaller than that in the forward direction in the most cases. The ε_p^{max} for $n_f = n_c$ substantially diminishes in comparison to that for $n_f = 2n_c$. The detailed values of ε_p^{max} and the maximum intensity of the proton beam I_p^{max} for each density n_f are shown in Table I.

Let us consider a reason why the highest proton energy depends on the plasma density n_f and why there is the optimal density. Figure 6 shows the maximum amplitude E_{max}^{ESF} of ESF observed on the target surfaces at 393 fs. As shown in Fig. 6, the maximum amplitude E_{max}^{ESF} in the backward seems

TABLE I. The numerical results of the particle energy of the protons emitted in the forward and backward directions at $t = 934$ fs. ε_p^{max} and ε_p^{avg} are the maximum and averaged values of the kinetic energy of the protons, respectively, and σ_p^{ene} is the standard deviation of the proton energy. Furthermore, the maximum intensity of the produced proton beam I_p^{max} at $t = 884$ fs is also shown.

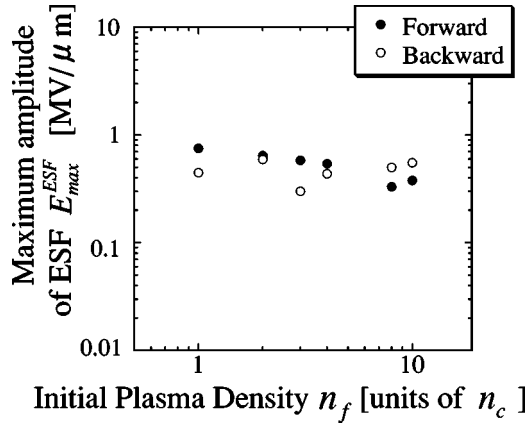| Plasma density	Kinetic energy of protons			Maximum intensity	Total protons emitted
n_f (units of n_c)	ε_p^{max} (MeV)	ε_p^{avg} (MeV)	σ_p^{ene} (MeV)	I_p^{max} (10^{16} W/cm^2)	(10^{20} protons/s/μm^2)
			Forward		
1	2.74	0.232	0.286	7.18	3.40
2	3.73	0.425	0.409	22.4	10.1
3	2.92	0.273	0.288	18.4	7.92
4	2.05	0.160	0.182	14.3	5.66
8	0.519	0.0341	0.0388	2.88	2.79
10	0.370	0.0252	0.0272	2.49	2.64
			Backward		
1	2.23	0.226	0.270	6.29	3.37
2	2.89	0.474	0.401	15.5	6.39
3	2.23	0.348	0.308	12.0	5.04
4	1.63	0.200	0.215	8.67	3.56
8	0.582	0.0361	0.0556	2.77	2.26
10	0.534	0.0292	0.0477	2.47	2.45

FIG. 6. The maximum amplitude of the ESF E_{max}^{ESF} observed on the forward and backward surfaces at 393 fs.

to be independent of the initial plasma density. Even in the forward direction, E_{max}^{ESF} decreases with increasing n_f simply and there is no optimal density. Why is there the optimal density for the maximum proton energy? To answer this question, let us show the actual electrostatic field felt by the highest-energy protons. For a comparison between E_x^{ESF} for the optimal density $2n_c$ and the others, Fig. 7 shows the electrostatic field $E_x^{ESF}(X_p(t))$ (solid curves) felt by the highest-energetic proton in the forward direction.

The E_x^{ESF} at $n_f > 2n_c$ is smaller than that at the optimal density $n_f = 2n_c$, the excited E_x^{ESF} is not sustained for a long time and diminishes rapidly for $n_f = n_c$ compared with that for $n_f = 2n_c$. Thus, the energy gain of the proton from ESF, $\delta\varepsilon_p = \int E_x(X_p)dX_p$, becomes smaller for $n_f = n_c$ than that for the optimal density $n_f = 2n_c$. What does cause this difference of ESF sustainment? In Fig. 7, the number of the heading electrons N_e^{out}, which exist at the outer region beyond the highest-energetic proton, is represented by dashed curves. As shown in each figure in Fig. 7, the time development of N_e^{out} agrees well with the evolution of $E_x^{ESF}(X_p(t))$, and this fact supports that the sufficient electron supply is crucial to keep the E_x^{ESF} field. Figure 8 shows example electron trajectories in the x direction for $n_f = 2n_c$. As shown in Fig. 8, the electrons oscillate in the potential well of ESF with a high frequency. Then, only a part of the electrons is energetic enough to get over the potential well, can reach the outer region of the accelerating protons, and sustain ESF to accelerate the high-energy protons. Therefore, the electron energy is crucially important to sustain the ESF and determine the final energy of the protons accelerated.

Figure 9 shows time developments of energy components in the computational domain. In each figure, lines with white and black circles represent the total kinetic energy of the protons and the electrons, respectively. Solid and dashed curves represent the total energy of the magnetic field $\int\int (1/2\mu_0)B_z^2 dxdy$ and the electric field $\int\int \frac{1}{2}\varepsilon_0(E_x^2 + E_y^2)dxdy$, respectively. In the cases of $n_f = n_c$ and $n_f \geq 10n_c$, the laser deposits its energy to the electrons only during the laser illumination, and the electron energy does not increase after the laser termination. On the other hand, in the cases of $n_f = 2n_c, 3n_c, 4n_c$, the laser excites the electric
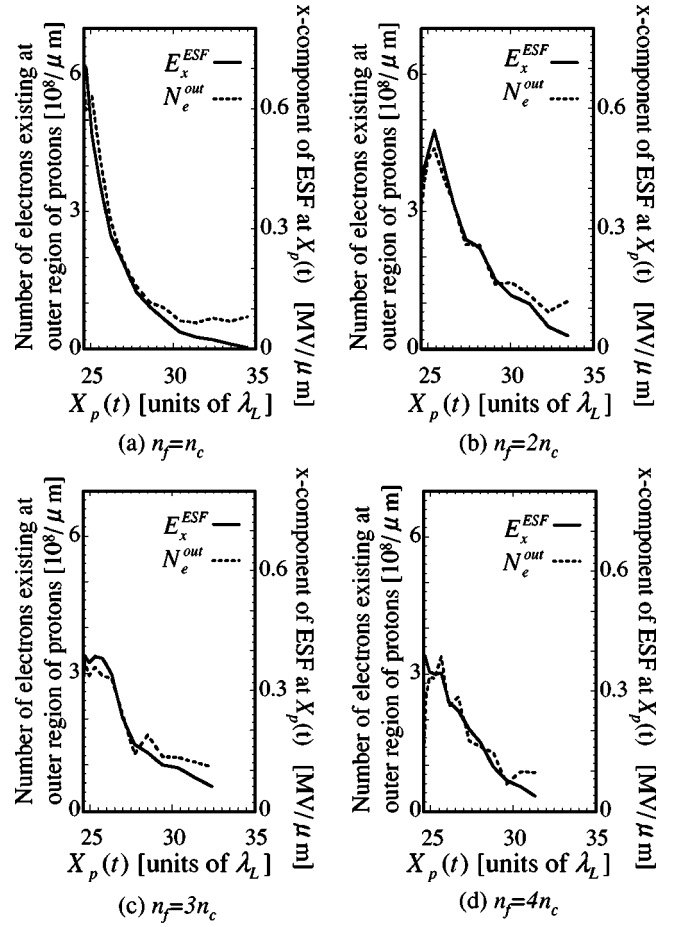

FIG. 7. The x component of electrostatic field $E_x^{ESF}(X_p(t))$ (solid curves) felt by the most energetic proton in the forward direction and the number of the electrons $N_e^{out}(X_p(t))$ heading the ESF (dashed curves) as a function of the position of the most-energetic proton $X_p(t)$. In the simulations, the uniformity in the z direction is assumed and N_e^{out} is estimated as the number of electrons per 1-μm thickness in the z direction.
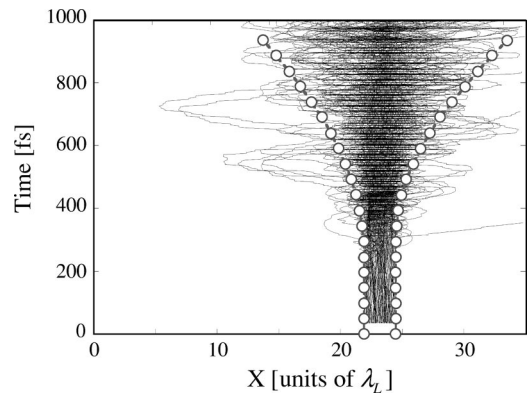

FIG. 8. Trajectories of the electrons heading the protons in the x direction for $n_f = 2n_c$. Some electrons move beyond the ESF potential well and contribute to create the expanding ESF wave. White circles show the trajectories of the most-energetic protons. As shown in Fig. 4, the trajectories of the protons agree with the positions of the ESF waves.
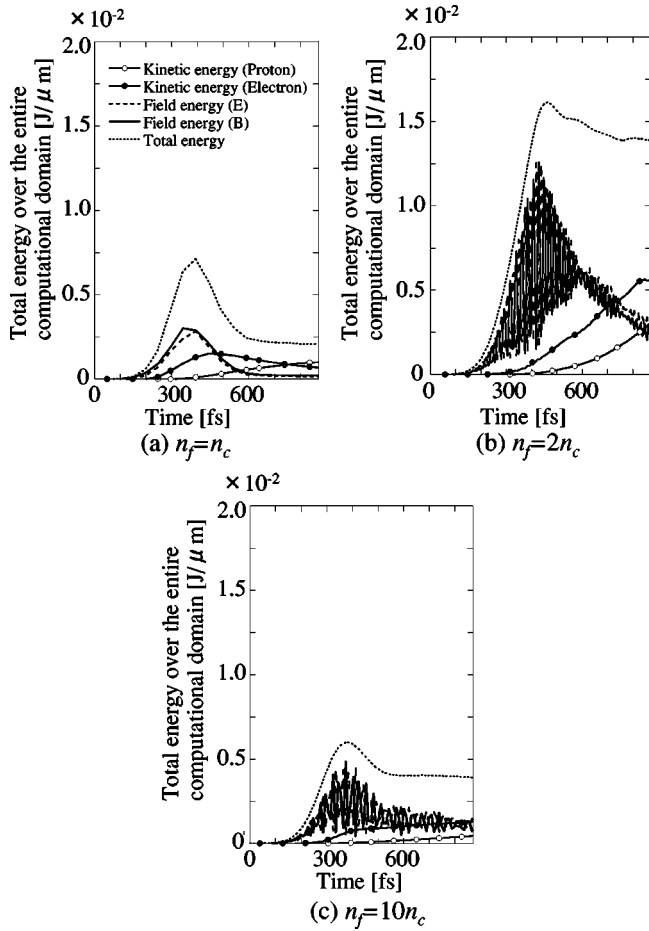
FIG. 9. Time development of the kinetic and field energies. In the simulations, the uniformity in the z direction is assumed and the total energy of the electrons is the value per 1 μm thickness in the z direction. At $\sim$393 fs, the maximum intensity of the incident laser 1.6×10^{19} W/cm^2 is illuminated on the target surface with a laser pulse duration $\tau = 300$ fs.

and magnetic fields and deposits its energy to the electric and magnetic fields, in addition to the electrons. In these cases, the electron energy increases by continuous energy transferences from the electric and magnetic fields to the electrons, even after the termination of the laser illumination. At the end of the computation, the total energy of the electrons becomes 4–6 times larger than of $n_f = n_c$. This continuous increase of the electron energy results in the sufficient supply of the electrons energetic enough to get over the ESF potential well and sustainment of the strong ESF even after the laser illumination ends.

C. Energy storage by the excitation of the magnetic and electric fields

In order to find a reason why the difference in the energy storage by the magnetic and electric fields shown in Fig. 9, the mechanism of the laser energy deposition and the excitation of the electric and magnetic fields are investigated.

Figure 10 shows the laser field at $t = 394$ fs. While the incident laser stops and is reflected at the plasma surface and
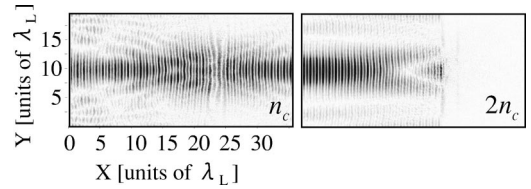

FIG. 10. The laser illumination on a slab plasma. The magnetic field B_z of the laser fields at $t = 394$ fs is represented for the initial slab plasma densities $n_f = n_c$ and $2n_c$. Except for $n_f = n_c$, the incident laser is cut off near the surface of the slab plasma.

the electromagnetic wave is cut off at the skin depth δ_{skin} for $n_f \gtrsim 2n_c$, the laser penetrates the target plasma for $n_f = n_c$ due to the relativistic effect [21]. Therefore, it is expected that when $n_f = n_c$, the electrons gain less energy from the incident laser field. Figure 11 shows electron maps in the x-p_x phase space. The panels (a), (b), and (c) show the electron maps at 295 fs, and the panels (d), (e), and (f) show those at 393 fs. As shown in the panels (a) and (d), when $n_f = n_c$, the incident laser accelerates the electrons in both the backward and forward directions, and the distribution is modified in the x direction corresponding to the wavelength of the incident laser λ_L. On the other hand, when $n_f \gtrsim 2n_c$, the electron acceleration mechanism at the initial acceleration phase is quite different from that for $n_f = n_c$. The panels (b) and (e) in Fig. 11 show the electron maps for $n_f = 2n_c$. In this case, the energy deposition to hot electrons due to the ponderomotive force is dominant, because the target plasma is overdense [22,23]. Then, the electrons existing around the laser-illuminated surface are accelerated in the forward direction and the electrons move inside the target with the interval of $\lambda_L/2$ as shown in Fig. 11(e). However, for the higher density $n_f \gtrsim 8n_c$ shown in the panels (c) and (f) in Fig. 11, it is observed that the electrons accelerated in the forward direction are scattered near the laser-illuminated surface.

Figure 12 shows the x component of $\mathbf{J}^{avg}$, which is the current density averaged in the y direction around the laser-illuminated spot $|y - y_c| < r_{spot}$. As shown in Fig. 12(b), a
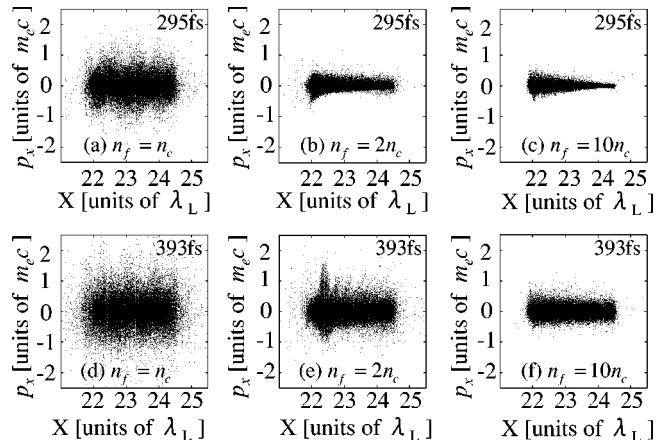

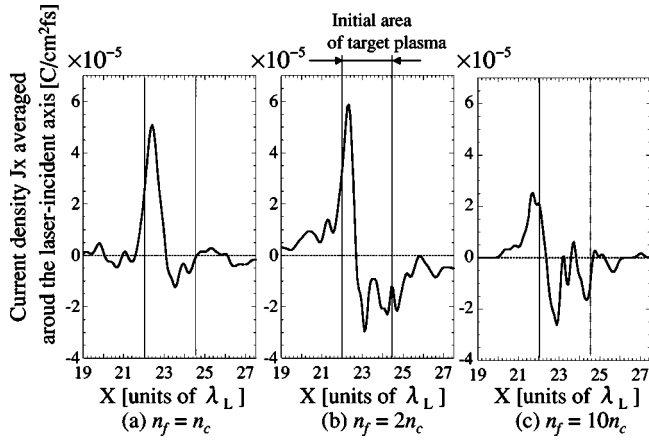FIG. 11. The electron maps in x-p_x space for $n_f = n_c$, $n_f = 2n_c$, and $n_f = 10n_c$.

FIG. 12. Current density $J_x(x)$ averaged in the y direction over $|y-y_c|<r_{spot}$ at 494 fs for (a) $n_f=n_c$, (b) $2n_c$, and (c) $10n_c$.

strong negative current in the target plasma due to the electrons propagating toward the forward side is observed for $n_f=2n_c$, $3n_c$, and $4n_c$, while there is no clear negative current piercing the target slab plasma for $n_f \gtrsim 8n_c$ and n_c. The strong negative current propagating in the target toward the forward direction creates an additional magnetic field inside the target plasma. Figure 13 shows the absolute value of the magnetic field $|B_z^{avg}|$ averaged in the time for one laser period at 393 fs. For all the initial plasma densities, the strong "surface" magnetic fields are excited on both the target surfaces due to the energetic electrons escaping from the target surfaces. In addition to the "surface" magnetic fields, an additional strong magnetic field in the target plasma is excited due to the inner electron flux for $n_f=2n_c$, $3n_c$, and $4n_c$ as shown in Fig. 13(b). This additional "inner" magnetic field has an opposite sign to the "surface" magnetic field excited on the laser-illuminated surface [see Fig. 14(a)]. The amplitude of the "inner" magnetic field reaches several kT as well as the "surface" magnetic fields when $n_f=2n_c$. This additional strong "inner" magnetic field also stores the
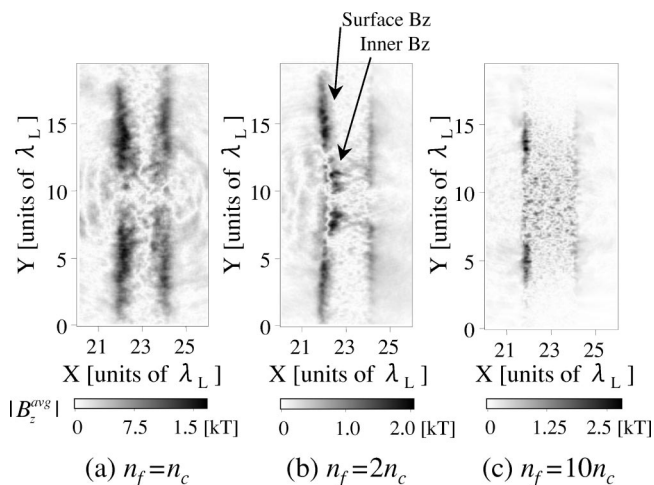

FIG. 13. Magnetic field excited for (a) $n_f=n_c$, (b) $2n_c$, and (c) $10n_c$ at $t=393$ fs. The absolute value of the magnetic field averaged in the time for one laser period is shown.

energy as the magnetic field energy. As shown in Fig. 14(a), the amplitude of the "inner" magnetic field increases even after ~ 393 fs, at which the maximum intensity of the incident laser is illuminated on the target plasma, and the maximum magnetic field 3.4 kT is observed at about 594 fs. For $n_f \gtrsim 8n_c$, the "inner" magnetic field is also excited. However, the electron accelerated by the ponderomotive force around the backward surface is scattered strongly in the target plasma as shown in Figs. 11(c) and 11(f), and the "inner" magnetic field is split into many small pieces likewise. Thus, there is not a large scale structure of the "inner" magnetic field as shown in Fig. 13(c). Actually, for $n_f=10n_c$, the simulation result shows that the amplitude of the excited inner magnetic field is one half of the "surface" magnetic field, that the excited "surface" magnetic field reaches the maximum value 2.2 kT at $t=393$ fs, and that the magnetic fields do not increase after the laser termination. The additional energy storage by the excitation of the "inner" magnetic field is considered to be one of the reason why the field energy for $n_f=2n_c$ increases drastically as shown in Fig. 9(b).

Next, let us investigate a mechanism of releasing the stored energy of the additional inner magnetic field. Figures 14(a) and 14(b) show the time development of the magnetic and electric fields, which are averaged in the time for one laser period, respectively, for $n_f=2n_c$. Furthermore, the time developments of the proton and electron density when
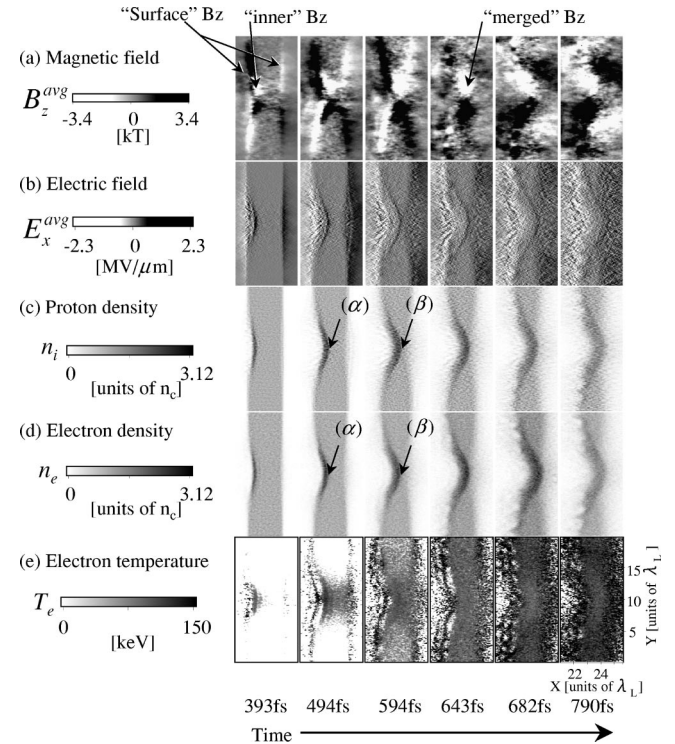

FIG. 14. Time development of (a) the magnetic field B_z averaged in the time for one laser period, (b) the electric field E_x averaged in the time for one laser period, (c) the proton density, (d) the electron density, and (e) the electric temperature T_e for $n_f=2n_c$. Here, positions X and Y are normalized by the laser wavelength λ_L. The positions (α) and (β) indicated by arrows coincide with the same positions shown in Fig. 15.
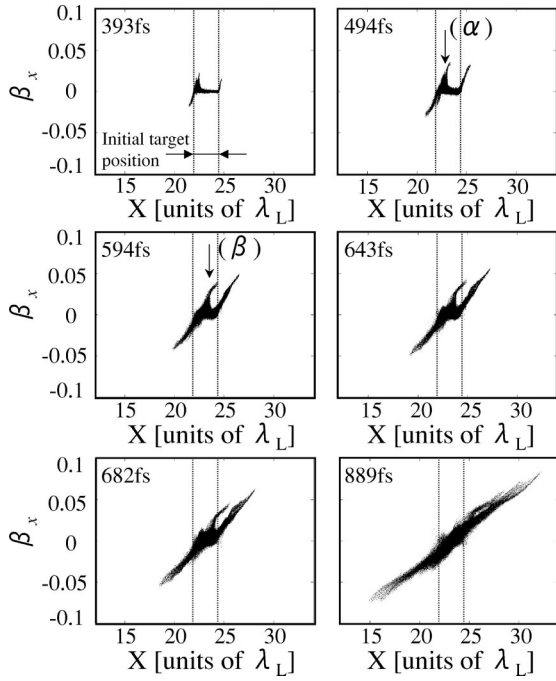
FIG. 15. Time development of the proton distribution in x-v_x phase space for $n_f = 2n_c$. Here, $\beta_x = v_x/c$. The positions (α) and (β) indicated by arrows coincide with the same positions shown in Fig. 14. In addition to the protons emitted outward from each surface, a group of the protons that are generated from the backward surface is accelerated to the forward surface, while moving inside the target plasma.

FIG. 16. The particle fluxes of proton and electron at (a) $t = 643$ fs and (b) $t = 692$ fs for $n_f = 2n_c$. Here, positions X and Y are normalized by the laser wavelength λ_L. For a comparison, the magnetic field B_z^{avg} averaged in the time for one laser period is also shown as contour plots in each panel.

$n_f = 2n_c$ are shown in Figs. 14(c) and 14(d), respectively. In the previous simulation result presented in Ref. [20], an excitation of a bisolitary wave, which consists of the strong electrostatic field and the charge separation, is observed inside the target surface. As shown in Fig. 14, it is also found that a pulse wave of E_x is excited and propagates with the inner magnetic field to the forward direction. At $t = 594$ fs, the inner magnetic field reaches the forward surface and merges with the surface magnetic field excited on the forward surface. Figure 15 shows the time development of the proton distributions in x-v_x phase space for $n_f = 2n_c$. As shown in Fig. 15, in addition to the protons emitted outward from each surface, some protons are generated near the backward surface and propagate together with the electric field of the pulse wave propagating in the target plasma to the forward surface. Here we call these protons the "lagged" protons. At about $t = 594$ fs, these protons accelerated by the pulse wave reach the opposite surface and run out. As shown in Fig. 16, the electrons accompanied by the lagged protons are pushed back to the target plasma from the forward vacuum region, because of the negative charge. The pushed back electrons make a detour around the "merged" magnetic field, which consists of the inner magnetic field and the surface magnetic field excited on the forward surface. The merged magnetic field interacts with the "pushed-back" electrons as shown in Fig. 16 and is forced back to the target backward surface [see Fig. 14(a)]. Then, the merged magnetic field also encounters the surface magnetic field existing
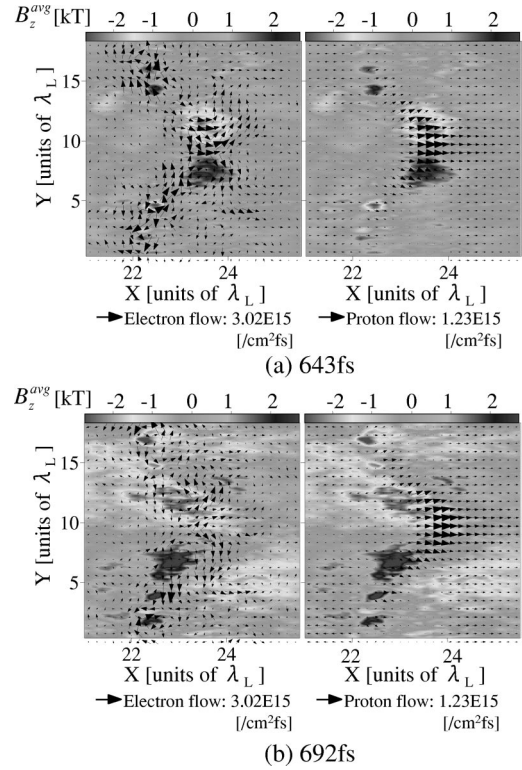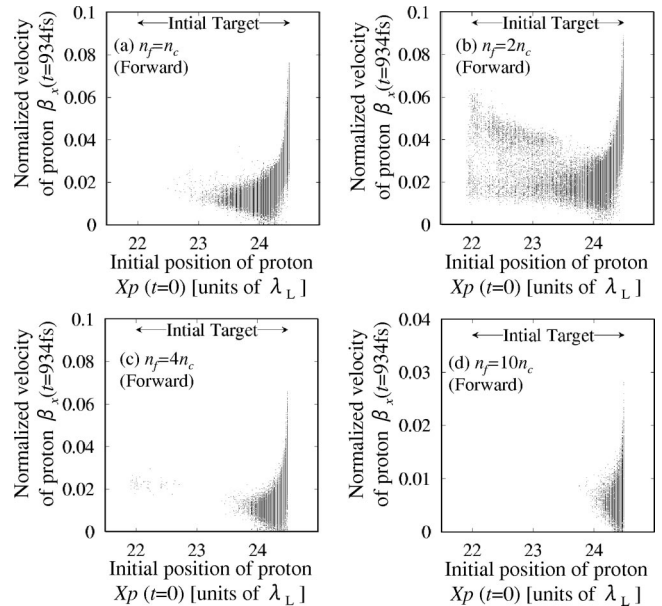

FIG. 17. The velocity v_x of the protons accelerated to the forward side at $t = 934$ fs vs the initial position of the protons $X_p(t = 0)$ for (a) $n_f = n_c$, (b) $n_f = 2n_c$, (c) $n_f = 4n_c$, (d) $n_f = 10n_c$. Here, β_x is v_x/c.
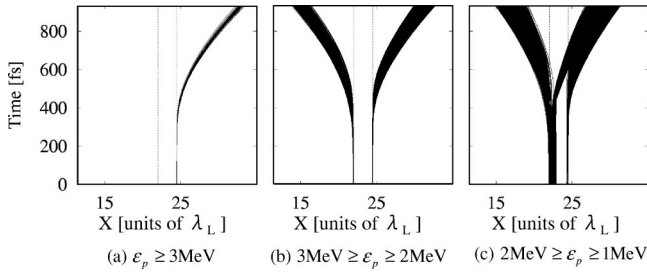
FIG. 18. The trajectories of the protons in the X-t plane for $n_f = 2n_c$. According to the kinetic energy of the each proton ε_p, the trajectories are sorted into (a) $\varepsilon_p \geqslant 3$ MeV, (b) 2 MeV $\leqslant \varepsilon_p < 3$ MeV, and (c) 1 MeV $\leqslant \varepsilon_p < 2$ MeV. In each panel, dashed lines represent the initial surface of the target plasma.

near the backward surface. Because the surface magnetic field has the opposite sign to the inner or merged magnetic field, a fragmentation occurs and the magnetic field is split into small pieces. This situation is similar to the magnetic reconnection process or the tearing mode instability [24], which accelerates electrons and protons along the boundary between the magnetic fragments. Actually, as shown in Fig. 14(e), the electrons are heated around the backward surface, at which the magnetic fragmentations occur. Through this process, the energy stored as the magnetic field is released and the electrons gain the energy. Thus, it seems that the excitation of the strong inner magnetic field is one of the reason why the total energy of the electrons increases even after the laser illumination ends as shown in Fig. 9(b), and why ESF is sustained well.

D. Origin of the protons

The dependence of the final velocity v_x of the protons accelerated to the forward side on the initial position is shown in Fig. 17. The vertical and horizontal axes of the figure are the velocity $\beta_x = v_x/c$ at $t = 934$ fs and the initial x positions of the protons $X_p(t=0)$, respectively. All proton particles accelerating in the forward direction are plotted on the $\beta_x - X_p(t=0)$ plane and the initial position of the target plasma is represented by the arrows in Fig. 17. As shown in the figure, the highest-energetic proton exists just on the surface at the initial time and almost all the energetic protons are generated from a thin layer on the target plasma surfaces for all the densities. This tendency of the position of the energetic protons agrees with the results of the experiment done by LLNL [1]. As shown in the above section, it is also reconfirmed that the lagged protons, which are generated from the backward surface of the target plasma, are accelerated while passing through the target plasma and go out of the forward side for $n_f = 2n_c$, $3n_c$, and $4n_c$ [20]. Figure 18 shows the trajectories of the energetic proton for $n_f = 2n_c$. As shown in Fig. 18, while the energetic protons are generated from a quite thin layer at the target plasma surfaces, there are other protons that are generated from the laser-illuminated surface and accelerated in the forward direction. The protons pass through the target plasma and go out of the forward plasma surface into the vacuum. This proton beam is the lagged proton beam described in the preceding section

and the acceleration of the lagged protons has been also shown in Fig. 15. The protons are accelerated by the ponderomotive force during the laser illumination, and then still accelerated even after the laser-illumination termination by the electric field of the excited pulse wave, as shown in Fig. 14. The generation of the lagged protons agrees with the previous results of the experiments and the simulation [2,4,20].

IV. SUMMARY

We studied the high-energy proton production from a slab plasma irradiated by a ultrashort high-power laser by the 2.5-dimensional electromagnetic particle-in-cell simulations. The simulation results show that the proton energy generated depends on the plasma density, and there is an optimal density. When a p-polarized laser beam of 1.6×10^{19} W/cm^2, 300 fs, $\lambda_L = 1.053$ μm, illuminates the slab hydrogen plasma, the optimal is obtained at the plasma density $n_f = 2n_c$ and the highest proton energy is 3.73 MeV in the parameter set values employed in this paper. The dependence on the plasma density is explained by the energy deposition from the laser to the electrons. It is reconfirmed that the electron acceleration sustained by the ponderomotive force takes an important role in the proton acceleration process.

For the overdense plasma, the incident laser is reflected on the plasma surface. The electrons existing around the laser-illuminated surface are accelerated in the forward direction violently by the ponderomotive force and the strong current piercing the target plasma is caused. This mechanism is similar to that reported by Yu *et al.* for a low-density plasma in front of a solid target [20]. In addition to the mechanism, it is pointed out in our work that for the optimal case the strong current piercing the target plasma excites the strong magnetic field inside the target plasma, and that the energy storage as the excited inner magnetic field contributes to the efficient proton acceleration.

Furthermore, Yu *et al.* [20] also pointed out that a bisolitary wave of the strong electrostatic field and the energetic protons has been observed. In this paper, it is found that the excited inner magnetic field propagates in the forward direction in the target plasma. After the inner magnetic field reaches the opposite surface, the inner magnetic field turns back, and breaks into the small fragments and releases its field energy to the electrons continuously even after the laser termination. In the future, the relation between the bisolitary wave and the inner magnetic field propagation should be studied further. For the parameter value set employed in this paper, this energy storage mechanism of the magnetic field takes an important role to accelerate proton acceleration effectively as well as the efficient energy deposition of the laser to the electrons.

[1] R.A. Snavely *et al.*, Phys. Rev. Lett. **85**, 2945 (2000).

[2] A. Maksimchuk, S. Gu, K. Flippo, D. Umstadter, and V.Y. Bychenkov, Phys. Rev. Lett. **84**, 4108 (2000).

[3] E.L. Clark *et al.*, Phys. Rev. Lett. **84**, 670 (2000).

[4] K.A. Tanaka, *et al.*, Phys. Plasmas **7**, 2014 (2000).

[5] S. Kawata, A. Manabe, and S. Takeuchi, Jpn. J. Appl. Phys., Part 1 **28**, 704 (1989).

[6] S. Kawata, T. Maruyama, H. Watanabe, and I. Takahashi, Phys. Rev. Lett. **66**, 2072 (1991).

[7] S. Kawata, T. Sato, T. Teramoto, E. Bandoh, Y. Masubichi, and I. Takahashi, Laser Part. Beams **11**, 757 (1993).

[8] K. Nemoto, A. Maksimchuk, S. Banerjee, K. Flippo, G. Mourou, D. Umstadter, and V.Yu. Bychenkov, Appl. Phys. Lett. **78**, 595 (2001).

[9] D. Umstadter, Phys. Plasmas **8**, 1774 (2001).

[10] R.W. Hockney and J.W. Eastwood, *Computer Simulation Using Particles* (McGraw-Hill, New York, 1981).

[11] T. Tajima, *Computational Plasma Physics* (Addison-Wesley, Redwood, CA, 1989).

[12] A.B. Langdon and B.F. Lasinski, Methods Comput. Phys. **16**, 327 (1976).

[13] *Computer Techniques for Electromagnetics*, edited by R. Mittra (Pergamon, New York, 1973).

[14] *Transient Electromagnetic Field*, edited by L. B. Felsen (Springer-Verlag, Berlin, 1976).

[15] S.C. Wilks, A.B. Langdon, T.E. Cowan, M. Roth, M. Singh, S. Hatchett, M.H. Key, D. Pennington, A. MacKinnon, and R.A. Snavely, Phys. Plasmas **8**, 542 (2001).

[16] T.Zh. Esirkepov, Y. Sentoku, K. Mima, K. Nishihara, F. Califano, F. Pegoraro, N.M. Naumova, S.V. Bulanov, Y. Ueshima, T.V. Liseikina, V.A. Vshivkov, and Y. Kato, Pis'ma Zh. Eksp. Teor. Fiz. **70**, 80 (1999) [JETP Lett. **70**, 82 (1999)].

[17] S.J. Gitomer, R.D. Jones, F. Begay, A.W. Ehler, J.F. Kephart, and R. Kristal, Phys. Fluids **29**, 2679 (1986).

[18] A.P. Fews, P.A. Norreys, F.N. Beg, A.R. Bell, A.E. Dangor, C.N. Danson, P. Lee, and S.J. Rose, Phys. Rev. Lett. **73**, 1801 (1994).

[19] P.E. Young, G. Guethlein, S.C. Wilks, J.H. Hammer, W.L. Kruer, and K.G. Estabrook, Phys. Rev. Lett. **76**, 3128 (1996).

[20] W. Yu, V. Bychenkov, Y. Sentoku, M.Y. Yu, Z.M. Sheng, and K. Mima, Phys. Rev. Lett. **85**, 570 (2000).

[21] A. Pukhov and J. Meyer-Ter-Vehn, Phys. Plasmas **5**, 1880 (1998).

[22] S.V. Bulanov and F. Pegoraro, Phys. Plasmas **1**, 745 (1994).

[23] W.L. Kruer and K. Estabrook, Phys. Fluids **28**, 430 (1985).

[24] H.P. Furth, J. Killeen, and M. Rosenbluth, Phys. Fluids **6**, 459 (1963).